A function-separated design of electrode for realizing high-performance hybrid zinc battery

Yijun Zhong, Xiaomin Xu, Pengyun Liu, Ran Ran, San Ping Jiang, Hongwei Wu, and Zongping Shao*

Mr. Y. Zhong, Mr. X. Xu, Ms. P. Liu, Prof. S. P. Jiang, Prof. H. Wu, Prof. Z. Shao

Western Australian School of Mines: Minerals, Energy and Chemical Engineering (WASM-MECE), Curtin University, Perth, Western Australia 6102, Australia
E-mail: zongping.shao@curtin.edu.au

Dr. R. Ran, Prof. Z. Shao
State Key Laboratory of Materials-Oriented Chemical Engineering, College of Chemical Engineering, Nanjing Tech University, Nanjing 211816, P. R. China

Prof. S. P. Jiang

Fuels and Energy Technology Institute, Curtin University, Perth, Western Australia, 6102, Australia

Rechargeable hybrid zinc battery is developed for reaching high power density and high energy density simultaneously by introducing an additional alkaline Zn-transition metal compound (Zn-MX) battery function into rechargeable Zn-air battery. However, the conventional single-layer electrode design is impossible to satisfy the requirements of both a hydrophilic interface for facilitating ionic transfer to maximize the Zn-MX battery function and a hydrophobic interface for promoting gas diffusion to maximize the Zn-air battery function. To tackle this dilemma, here we propose a function-separated design which allocates the two battery functions to the two faces of the cathode. The electrode is composed of a hydrophobic MnS layer decorated with Ni-Co-S nanoclusters that allows for smooth gas diffusion and efficient oxygen electrocatalysis and a hydrophilic $Ni_xCo_{1-x}S_2$ layer that favors fast ionic transfer and superior performance for energy storage. The hybrid zinc battery operating with the function-separated electrode shows a high short-term discharge voltage of ~1.7 V, an excellent high-rate galvanostatic discharge-charge with a power density up to 153 mW cm^{-2} at 100 mA cm^{-2}, a good round-trip efficiency of 75% at 5 mA cm^{-2}, and a robust cycling stability for 330 h with an excellent voltage gap of ~0.7 V at 5 mA cm^{-2}.

1. Introduction

Buffering the fluctuated electric power supply from renewable resources and the uneven power utilization requires advanced electrochemical energy storage technologies.[1,2] While the commercially available Li-ion batteries (LIBs) can provide acceptable energy density, their widespread use remains questionable considering the high price of Li and the safety issue of organic electrolytes.[3,4] Therefore, alternative electrochemical energy storage devices which are both cost-effective and safe and have high energy density are highly demanded.[5-7] Zn-air batteries that use an aqueous alkaline solution as the electrolyte and abundant Zn as the anode have attracted considerable attention recently with a wide range of application potential, due mostly to their advantageous features of high energy density (1218 Wh kg^{-1}), high safety (no organic electrolyte), and low cost (cheap Zn raw material).[8-10] However, the performance of Zn-air batteries is strongly dependent on the air electrode, and most of the available Zn-air batteries show poor rate capability and round-trip efficiency due to the unsatisfactory cathode performance. Alkaline Zn-transition metal compound (Zn-MX) batteries (e.g., Zn-Co batteries, Zn-Ni batteries) are important categories of Zn-based batteries.[11] Some of the cathode materials (Co_3O_4[12], NiO[13]) for the Zn-MX batteries demonstrated higher discharge voltages than the conventional air cathodes for Zn-air batteries. By introducing the function of a Zn-MX battery into the air electrode of a Zn-air battery, a so-called hybrid Zn battery was proposed, which may show both high power density and excellent energy density.[14,15]

A typical hybrid Zn-based battery has a cathode-electrolyte-anode battery configuration similar to that of a Zn-MX battery or a Zn-air battery. The cathode, where both cation redox and oxygen redox occur, can have a great impact on the overall performance.[15-17] During the past, most of the efforts on hybrid Zn-based batteries were made on the electrochemical evaluation of the hybrid features and the development of multifunctional cathode materials (e.g., Co_3O_4[17-19], $NiO/Ni(OH)_2$[15,20,21],

WILEY-VCH

NiCo$_2$O$_4$[16,22], NiCo$_2$S$_4$[23,24], Ag[25,26]) with favorable cation redox capability and decent bifunctional catalysis towards both oxygen reduction reaction (ORR) and oxygen evolution reaction (OER).[27-29] Most hybrid batteries in these works presented single-layer electrodes with even dispersion of all functional components (catalyst/active material, conductive carbon and binder). The rational design of the electrode structure for improving the mass transfer on a hybrid Zn battery cathode may also have a considerable influence on the battery performance, which remains largely underexplored.

In some reports, cathode with optimized liquid-solid interfaces[30] and optimized gas-liquid-solid interfaces[31,32] has been demonstrated to enhance the overall performance of Zn-MX batteries and Zn-air batteries, respectively. The construction of a porous electrode with suitable pore size and pore distribution is a widely adopted strategy in Zn-air batteries and Zn-MX batteries, which can improve the mass transfer to some extent.[11,33-36] Another effective strategy for achieving fast mass transfer is through tuning the wettability (i.e., hydrophilicity or hydrophobicity) of the cathode.[30,37,38] The Faradaic cation redox in a Zn-MX battery cathode requires improved electrolyte accessibility for better ionic transfer[11] while the oxygen redox in a Zn-air battery cathode requires improved gas accessibility for accelerated gas diffusion[39]. The conventional single layer electrode design, however, can only meet one of the two requirements, i.e., establishing either a hydrophilic interface for facilitating ionic transfer or a hydrophobic interface for providing better gas diffusion. This contradiction leads to an inevitable sacrifice of the performance of one function in order to satisfy the other.

A separation of the two battery functions based on the above specific requirements, in the electrode scale, may resolve this contradiction. To achieve this separation, a double-face (Janus-type) electrode design with different properties on each face would be a promising method. In other electrochemical applications (e.g., electrochemical H$_2$O$_2$ production, fuel cells, electrocatalysis, and conventional rechargeable Zn-air batteries), Janus-type electrodes with an asymmetric double-

layered structure have demonstrated some unique improvement on the mass transfers and stability.[31,40-41] Some previous reports for oxygen electrocatalysis developed the Janus-type electrode with asymmetric wettabilities to facilitate the mass transfer for oxygen redox,[31,42] while some others proposed Janus-type electrodes with asymmetric compositions (e.g., MnO_2-NiFe layered double hydroxides) to improve the cycling stability of Zn-air batteries.[43,44] However, the above asymmetric designs for other applications only focus on specific reactions (e.g., ORR & OER) which may not achieve an effective improvement of both battery function of the hybrid Zn battery, especially for the Zn-MX battery function.

In this work, we propose a new function-separated design which allocates the two battery functions to the two faces of the electrode, respectively. The electrode perfectly tackles the dilemma between electrolyte accessibility and gas accessibility in a single-layer electrode and facilitates both oxygen redox and Faradaic cation redox at the same time. Specifically, a hydrophobic polytetrafluoroethylene (PTFE)-incorporated MnS layer with modification of Ni-Co-S nanoclusters provides outstanding electrocatalytic activity for ORR and OER as an air electrode for Zn-air battery and a $Ni_xCo_{1-x}S_2$ layer with a hydrophilic surface acts as the cathode of Zn-MX battery. Such an exquisitely designed electrode was fabricated based on a facile two-step process. Hybrid zinc batteries with the function-separation design of the electrode demonstrated advantageous features of high power density, excellent round trip efficiency and good stability.

2. Results and Discussion

2.1. Preparation and characterization of the function-separated electrode

Compared to the conventional single-layer electrodes (**Figure 1a&b**), the new function-separated design allocates the electrode layer face to the electrolyte for the Zn-MX battery function and the layer face to air for the Zn-air battery function. The achievement of the function-separated design includes two different aspects, i.e., asymmetric wettability and asymmetric composition. Based on

the rational design of the composition which facilitates kinetics of the redox reactions and the design of the wettability which facilitate the specific mass transfers (**Figure 1c**), both battery functions could be optimized. Noted that such function-separation focuses on the optimization at the electrode scale, and it does not conflict with the concept of the "hybrid Zn battery" where battery functions are still hybridized at the battery scale with only one Zn anode and one electrolyte, aiming at achieving both high power density and energy density in a single battery.

The fabrication procedure of such a function-separated electrode is schematically shown in **Figure 2a-c**. A layer consisting of MnO_2 nanosheets, carbon nanotube (CNT) and polytetrafluoroethylene (PTFE) with a mass ratio of 6:2:2 was first prepared (**Figure 2a**). Nickel-cobalt bimetallic layered double hydroxide (NiCo-LDH) was integrated to the MnO_2-CNT-PTFE layer by electrodeposition at a reduction current of 10 mA in a 0.05 M $Co(NO_3)_2$ + 0.05 M $Ni(NO_3)_2$ aqueous solution. During the electrodeposition process, NO_3^- was reduced while at the same time OH^- was generated and reacted with the Co^{2+} and Ni^{2+} to form NiCo-LDH that deposited within the pores of MnO_2-CNT-PTFE layer or on its surface.[45,46] It is important to note that the PTFE in the MnO_2-CNT-PTFE layer served not only as a binder, but also as a wettability tuning agent. The hydrophobic nature of the MnO_2-CNT-PTFE layer effectively suppressed accessibility of the $Co(NO_3)_2$ + 0.05 M $Ni(NO_3)_2$ solution during the electrodeposition process. As a result, only a small amount of NiCo-LDH was deposited inside the MnO_2-CNT-PTFE layer while the majority of the NiCo-LDH was deposited on the layer surface (**Figure 2b**). This design of distribution of Ni, Co species could provide two beneficial effects on the hybrid Zn batteries. On the one hand, sufficient pores were preserved for smooth gas diffusion and ionic transfer. On the other hand, the proper amount of NiCo-LDH deposition inside the layer could enhance the bifunctionality for oxygen electrocatalysis, which will be discussed in more detail later. It was reported that the electronic conductivity of manganese sulfide (e.g., α-MnS: ~1×10^{-1} S cm^{-1})[47] is ~5 orders of magnitude higher than manganese oxide (e.g., δ-MnO_2: ~2×10^{-6} S cm^{-1})[48] at room temperature. To achieve a higher electronic conductivity of the electrode material for better charge

transfer, the resulting dual-layer electrode was further sulfurized using a facile thermal treatment with sulfur vapour at 350 °C (**Figure 2c**), where MnO_2 was converted into MnS and NiCo-LDH was converted into $Ni_xCo_{1-x}S_2$.

According to the results in **Figure 2d&e**, the different hydrophilic/hydrophobic properties of the different layers in the electrode were confirmed by contact angle analysis with the liquid electrolyte for the hybrid Zn batteries. For the $Ni_xCo_{1-x}S_2$ layer, a contact angle of 82° was observed suggesting its hydrophilic character. As to the MnS layer, however, a much larger contact angle of 148° was observed, suggesting its hydrophobic nature, as expected. **Figure 2f&g** gives the surface morphology and element mapping of the sulfurized electrode based on the analysis from scanning electron microscope and energy-dispersive X-ray spectroscopy (SME-EDS). The dual-layer feature with Ni-, Co-rich hydrophilic layer and a Mn-rich hydrophobic layer was revealed according to the Ni, Co and Mn dispersion within the electrode. Cracks with a width around tens of micrometers were observed on the top $Ni_xCo_{1-x}S_2$ layer. Such cracks may form during the drying process of the deposited LDH (**Figure S1a**), likely due to the mismatched shrinkage of the bottom layer and the loose and porous hydrophilic layer (**Figure S1d** & inset image of **Figure 2f**). It is worth noting that firm attachment of the top $Ni_xCo_{1-x}S_2$ layer onto the bottom layer was realized owing to the presence of strong interaction between the Ni, Co species and the surface CNT and PTFE (**Figure S1b&c**). The thickness of the hydrophilic layer and the hydrophobic layer are ~15 and ~60 µm, respectively, as observed with a SEM of the cross-section of the electrode (**Figure 2h**). The cross-layer linear scan EDS profile of the electrode cross-section (**Figure 2i**) provided further supportive evidence of the dispersion of Mn and Co-Ni compounds (**Figure 2g**).

The phase composition of the electrode was first characterized by X-ray diffraction (XRD, **Figure 3a**). A cubic phase with an *Fm$\overline{3}$m* space group was observed for the hydrophobic layer, which matched well with the standard powder diffraction file (PDF, code 03-065-0891) of MnS, while a

cubic phase with a $Pa\overline{3}$ space group was observed for the hydrophilic layer, which is well assigned to a phase similar to cubic CoS_2 (PDF code 00-041-1471). The phase composition of the two different electrode layers was further investigated by high-resolution transmission electron microscopy (HR-TEM) presented in **Figure 3b,c,e,f**. Crystalline phase with lattice distances of 0.23 and 0.25 nm was observed in the hydrophilic layer, which can be assigned to the $(21\overline{1})$ and (012) lattice planes of $Ni_xCo_{1-x}S_2$ phase. As to the hydrophobic layer, crystalline phase with lattice distance of 0.26 and 0.26 nm was observed, which matched well with (200) and (020) planes of MnS. Both XRD and HR-TEM results confirmed the different compositions of the two layers in the electrode. The TEM-EDS elemental mapping provided more details about the materials composition (**Figure 3d&g**). As expected, a minor amount of Ni-Co-S nanoclusters was deposited on the MnS nanoparticles and well dispersed within the hydrophobic layer (**Figure 3g**). It should be mentioned that owing to the strong background signal from MnS, the phase structure of the Ni-Co-S nanoclusters within the hydrophobic layer was difficult to be determined.

2.2. Bifunctional catalytic activity for ORR-OER and performance of the Zn-air battery function

Both the intrinsic catalytic activity of the electrocatalyst and the gas diffusion properties of the electrode determine the performance of the air electrode in a Zn-air battery.[38,39,49,50] The intrinsic catalytic activity of MnS and $Ni_xCo_{1-x}S_2$ for ORR and OER was assessed using a rotating disk electrode (RDE, 1600 rpm) based setup with a 0.1 M KOH electrolyte (See detailed preparation procedures and characterizations in Supporting Information and **Figure S2**). According to **Figure 4a**, MnS shows favourable catalytic activity of ORR with a half-wave potential ($E_{1/2}$) of 0.851 V (iR-corrected, vs RHE), which is comparable to that of the commercial Pt/C + IrO_2 catalyst ($E_{1/2}$ = 0.854 V). An electron transfer number of 3.97 between 0.4 and 0.8 V vs RHE was presented for the ORR of the MnS (**Figure S3**). The transfer number of ~4 indicates the predominant 4-electron transfer process for OH^- yielding.[51-53] MnS also shows a fair OER activity with a potential of 1.813 V at 10 mA cm^{-2} ($E_{j=10}$). While the ORR activity of $Ni_xCo_{1-x}S_2$ ($E_{1/2}$ = 0.710 V) is inferior to MnS, $Ni_xCo_{1-x}S_2$ material shows a

more favourable OER activity indicated by an $E_{j=10}$ of 1.610 V. It suggests that the introduction of $Ni_xCo_{1-x}S_2$ into the MnS will realize a significant improvement of the OER activity. The voltage gap (ΔE) between $E_{j=10}$ for ORR and $E_{1/2}$ for OER indicates the bifunctionality of the oxygen catalysts. Indeed, the MnS-$Ni_xCo_{1-x}S_2$ mixtures (physically mixed) with a wide range of weight ratio from 4:1 to 1:2 demonstrated smaller ΔE from 867 to 813 mV (**Figure 4b**), which are all better than single component MnS(ΔE =962 mV), $Ni_xCo_{1-x}S_2$ (ΔE =900 mV) and a mixture of benchmark commercial Pt/C + IrO_2 catalysts (ΔE =882 mV), demonstrating the superiority of MnS-$Ni_xCo_{1-x}S_2$ as a bifunctional electrocatalyst for Zn-air batteries. This result indicates that even a small amount of $Ni_xCo_{1-x}S_2$ decoration on the MnS could lead to a significantly improved bifunctionality for oxygen catalysis. It is noted that the above results were achieved by physical mixing of MnS and $Ni_xCo_{1-x}S_2$ powders. Improved activity of oxygen catalysis for the function-separated electrode is expected considering that better dispersion of Ni-Co-S nanoclusters on the MnS was achieved by the wettability-selective electrodeposition as discussed.

The performance of the function-separated electrode in real Zn-air battery was then evaluated using a home-constructed Zn-air battery model with an alkaline electrolyte and a metallic Zn anode. For comparison, a similar MnS electrode without the electrodeposition of $Ni_xCo_{1-x}S_2$ was also investigated. In cyclic Voltammetry (CV) scans as shown in **Figure 4c**, the function-separated MnS-$Ni_xCo_{1-x}S_2$ electrode demonstrated a similar ORR (discharging) onset voltage to the MnS electrode. However, a much-increased current response for OER (charging) was demonstrated for the function-separated MnS-$Ni_xCo_{1-x}S_2$ electrode. Considering the possible overlap of the current response of the cations redox and of the OER in the CV scans, galvanostatic (5 mA cm^{-2}) charging (30 min)-discharging (30 min) technique was applied to avoid the interfere from cation redox. As shown in inset image in **Figure 4d**, in every galvanostatic charging and discharging, Zn-MX battery function contributed by the cation redox happens first and presents a lower charging voltage and a higher discharge voltage. Once the cation redox is completed, the subsequent voltage profile represents

8

the actual working voltages of Zn-air battery function. The median charging voltage (V_C) and the median discharging voltage (V_D) located after the completion of cation redox provide a better evaluation of the actual performance of the Zn-air battery function. The battery with the function-separated MnS-Ni$_x$Co$_{1-x}$S$_2$ electrode (with a MnS and Ni$_x$Co$_{1-x}$S$_2$ loading of ~2 and ~0.8 mg cm^{-2}, respectively) showed a high V_D of 1.930 V and a low V_C of 1.260 V in the 2nd cycle (**Figure 4d**), corresponding to a voltage gap ($\Delta V_{Zn-air} = V_C - V_D$) of only 670 mV. For comparison, similar electrode with only MnS or only Ni$_x$Co$_{1-x}$S$_2$ prepared by a similar method showed an inferior ΔV_{Zn-air} of 702 mV and 737 mV in the 2nd cycle, respectively. The lower ΔV_{Zn-air} of the MnS-Ni$_x$Co$_{1-x}$S$_2$ than the single material (MnS or Ni$_x$Co$_{1-x}$S$_2$) electrodes further confirmed the beneficial effect from the Ni-Co-S nanocluster deposited within the hydrophobic MnS layer for facilitating OER. A prolonged cycling test of the battery at 5 mA cm^{-2} was presented in **Figure 4e**. In the first 100 cycles, the ΔV_{Zn-air} kept almost unchanged (672 mV in 100th cycle, 670 mV in 2nd cycle). A very good ΔV_{Zn-air} of 760 mV still remained at the 330th cycle. (**Figure 4e**). The battery also showed good ΔV_{Zn-air} of 743 mV and good cycling stability for 200 h at a higher current density of 10 mA cm^{-2}.

2.3. Performance of the Zn-MX battery function and optimization of the function-separated electrode

The electrochemical character of Zn-MX battery function for the function-separated electrode was evaluated by CV scans at a wide voltage window of 0.8-2.2V vs Zn. As shown in **Figure 4c**, a broad peak couple was presented within the voltage window from ~1.5 to ~2.0 V, which could be mainly attributed to the redox couples of Ni^{2+}/Ni^{3+} and Co^{2+}/Co^{3+} in Ni$_x$Co$_{1-x}$S$_2$.[54-57] The reversible discharge/charge reaction of Ni$_x$Co$_{1-x}$S$_2$ may follow the reactions:

$$Ni_xCo_{1-x}S_2 + OH^- \leftrightarrow Ni_xCo_{1-x}S_2OH + e^- \tag{1}$$
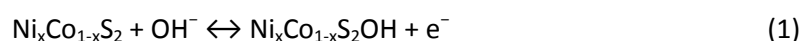
The function-separated electrodes with higher Ni$_x$Co$_{1-x}$S$_2$ loadings (achieved by controlling the deposition time of NiCo-LDH) demonstrated significantly larger capacity at higher potential range

(300 s deposition, ~0.15 mA cm^{-2} at voltage >1.5 V) than the electrode with less (60 s deposition, ~0.10 mA cm^{-2}) or no Ni$_x$Co$_{1-x}$S$_2$ deposition (**Figure 5a&b**). It is noted that MnS also presented the partial contribution to the capacity, while its contribution was not as significant as Ni$_x$Co$_{1-x}$S$_2$ and such capacity is presented at lower voltage range.[58,59] Indeed, increasing the loading of MnS from 0 to 3 mg did not significantly improve the capacity at the high voltage range (**Figure 5c**). Since the power density and energy density of the Zn-MX battery is highly associated with the working voltage which is related to the electrode material, the higher discharge potential of Ni$_x$Co$_{1-x}$S$_2$ is thus more favourable compared with the MnS.

The above performance results of the Zn-air battery function and Zn-MX battery function with the function-separated MnS-Ni$_x$Co$_{1-x}$S$_2$ electrode confirms our hypothesis on the asymmetric compositional design. Based on this understanding, the electrode was further optimized by variating the loading of MnS and Ni$_x$Co$_{1-x}$S$_2$. With an optimized MnS loading of 3 mg cm^{-2} and NiCo-LDH deposition time of 300 s (**Figure S4**), a ΔV_{Zn-air} of 659 mV (**Figure 5b**) and a capacity of Zn-MX battery (C$_{Zn-MX}$, approximately determined by the intersection of the two tangent lines on the deep-slope side representing the Zn-MX battery function and the flat side at ~1.3 V representing the Zn-air battery function in the galvanostatic discharge profiles) reached ~0.27 mAh cm^{-2} (**Figure 5c**) in the 2nd cycle, with round-trip efficiency (energy efficiency) of 69% (**Figure 5b**).

The optimized electrode also demonstrated excellent high-rate-performance for both battery functions. A lower cut-off-capacity (1 mAh cm^{-2}) was then set for the high-rate-performance test to highlight the improvement of round-trip efficiency resulted from the Zn-MX battery function. As presented in **Figure 5d**, ΔV_{Zn-air} of 586, 635, 687, 757 and 906 mV for the Zn-air battery function were achieved at 2, 5, 10, 20, 50 mA cm^{-2}, respectively. Even at a very high current density of 100 mA cm^{-2}, a fair ΔV_{Zn-air} of 1101 mV was presented. Good rate retention with a ΔV_{Zn-air} of 585 mV was also achieved when the current density decreased back to 2 mA cm^{-2}. The round-trip efficiency of the

10

WILEY-VCH

hybrid battery reaches 76% and 74% at 2 and 5 mA cm^{-2}, respectively. For comparison, the round-trip efficiency of the Zn-air battery function only (V$_{Zn-air}$ efficiency, evaluated by the median discharge/charge voltages, **Figure 6d**) is 67% at 5 mA cm^{-2}. As compared in **Figure 6d**, although a Pt/C + IrO$_2$ electrode demonstrated similar ΔV_{Zn-air} and V$_{Zn-air}$ efficiency to the function-separated MnS-Ni$_x$Co$_{1-x}$S$_2$ electrode, the energy efficiency of the Pt/C + IrO$_2$ electrode (66%) is much inferior. Although increased overpotentials of the Zn-MX battery function were observed when the current density was higher than 10 mA cm^{-2} (**Figure 5e**), the increase was much insignificant than those of the Zn-air battery function. This result suggests the benefits from the integration of the Zn-MX battery function for improving power density, especially at high current densities. The direct comparison of power densities profiles of the two electrodes at different constant discharging current (5-100 mA cm^{-2}) are presented in **Figure 5f**. In a short-term discharging situation (e.g., discharge energy < 0.1 mAh cm^{-2}), the hybrid battery with the function-separated electrode provide ~50% higher power density (153 mW cm^{-2}) than that with a conventional Pt/C + IrO$_2$ electrode (103 mW cm^{-2}) at 100 mA cm^{-2}. As discussed in the Introduction section, Zn-based battery is a promising technique designed for buffering the unpredictable fluctuating electricity supply from renewable energy resources and unstable electricity consumption. Such a short-term sensitive, high-power-density, high-energy-efficiency and highly reversible performance of the function-separated electrode is exactly suitable for this purpose.

Moreover, the optimized electrode presented a favorable stability over 200 h (**Figure 5b**), which was more stable than the Pt/C + IrO$_2$ electrode (**Figure S5**). It is interesting that the increased loading of Ni$_x$Co$_{1-x}$S$_2$ also had a positive impact on the stability of the battery performance as presented in **Figure 5b**. This could be ascribed to the alleviation of the loss of Mn compounds by Ni$_x$Co$_{1-x}$S$_2$. During the discharging-charging process, MnS could partially dissolve in the strong alkaline electrolyte,[60,61] which could result in the deterioration of discharge overpotentials. On the one hand, the partial coverage of Ni$_x$Co$_{1-x}$S$_2$ on the MnS surface provided physical blockage for alleviating the diffusion of

the dissolved Mn species. On the other hand, the $Ni_xCo_{1-x}S_2$ may provide a redox-active surface for facilitating the re-deposition of the dissolved Mn species.[62] The above excellent high-rate galvanostatic charge-discharge performance and good cycling stability of the function-separated $MnS-Ni_xCo_{1-x}S_2$ electrode are better than most advanced cathodes for hybrid Zn batteries[15-18,23,26,29] and for Zn-air batteries[31,63-72], as compared in **Table S1**.

2.4. Important role of the asymmetric wettability design in the function-separated electrode

To verify the beneficial effect for both gas diffusion and ionic transfer from the function-separated design as illustrated in **Figure 1**, performance of hybrid Zn battery with the function-separated electrode was further compared with the conventional single-layer electrodes with similar MnS and $Ni_xCo_{1-x}S_2$ loading. The wettability of the single-layer electrodes was modified by using different binders (hydrophilic Nafion and hydrophobic PTFE, **Figure 6b**) and their combination (1:1 wt:wt). A more hydrophilic electrode (e.g., electrode with Nafion) presented a higher C_{Zn-MX}, at the same time, however, a larger ΔV_{Zn-air} (**Figure 6a**). This result provides clear evidence that the inevitable contradiction of wettability design if a conventional single-layer design is applied. The as-designed optimized function-separated $MnS-Ni_xCo_{1-x}S_2$ electrode demonstrated both a higher C_{Zn-MX} (0.27 mAh cm^{-2}) and a significantly smaller ΔV_{Zn-air} (659 mV) (**Figure 6c**), compared to a single layer electrode with a balanced performance (Nafion+PTFE: 0.15 mAh cm^{-2} and 692 mV). As a result, the energy efficiency of the function-separated electrode (69%) was higher than all the tested single-layer electrodes (PTFE: 66%, Nafion:66%, PTFE+Nafion: 67%). In addition, owing to the exquisite decoration of Ni-Co-S nanoclusters and the top-covered $Ni_xCo_{1-x}S_2$ on the MnS layer, the function-separated electrode showed better voltage and energy efficiency retention in the prolonged 200-cycle performance (**Figure S6**).

3. Conclusion

In summary, a function-separated design of electrode with unique compositional distribution and distinguishing wettability on the two different layers was proposed for realizing high-performance hybrid Zn batteries. The electrode design perfectly tackles the dilemma between electrolyte accessibility and gas accessibility in a conventional single-layer electrode and facilitates both cation redox and oxygen redox. As a result, both functions of Zn-air battery and Zn-MX battery were optimized simultaneously, demonstrating advantageous features of high power density, excellent round trip efficiency and superior cycling stability. The concept of function-separated electrode design also provides opportunities for further optimizing redox reactions and multiple mass transfers in cathodes with other advanced active materials and catalysts (e.g., Ag/AgO$_x$, simple or complex Mn/Co/Ni-based metal hydroxides/oxides/sulfides) for hybrid Zn batteries. The design could also provide inspiration for the development of other electrodes with complicated ionic and gas transfer situations, e.g., proton-exchange membrane fuel cells and metal-air batteries.

4. Experimental Section

Preparation of MnO$_2$-CNT-PTFE film: The MnO$_2$-CNT-PTFE (with a mass ratio of 6:2:2) film was prepared by ultrasonic mixing 0.06 g MnO$_2$ (detailed synthesis see Supporting Information), 0.02 g CNT, 3.33 g 0.6 wt% PTFE solution (containing 0.02 g of PTFE) and 10 mL of ethanol. The mixed dispersion was dried at 60°C and wetted with a small amount of ethanol again to form a gum-like mixture. The gum was pressed into a thin film and dried at 60 °C, resulting in a dry film with an areal MnO$_2$ loading amount of ~2 to 3 mg cm^{-2}. Small round disks with a diameter of 8 mm and an area of 0.5 cm^2 were cut using a hole puncher.

Preparation of function-separated MnS-Ni$_x$Co$_{1-x}$S$_2$ electrode: The electrode was prepared with a two-step procedure. First step is the electrodeposition of NiCo-LDH on the MnO$_2$-CNT-PTFE film.

13

Typically, MnO_2-CNT-PTFE film was cold pressed on one side of a stainless-steel mesh current collector. The MnO_2-CNT-PTFE electrode and a graphite electrode were soaked in a 0.05 M $Co(NO_3)_2$ + 0.05 M $Ni(NO_3)_2$ aqueous solution to establish a two-electrode system. A constant reduction current (10 mA) was applied on the working electrode with a duration time of 60-300 s. The double-layer electrode after deposition (NiCo-LDH on MnO_2-CNT-PTFE) was removed from the solution and flushed with deionized water and then dried at ambient atmosphere. The second step is the sulfurization of the double layered electrode. The electrode was put in one end of a 3x6 cm alumina boat while 0.1 g of sulfur powder was put on the other end. The boat was covered by another empty alumina boat and then placed into a glass tube in a tube furnace. A heating treatment of 350 °C for 0.5 h with a fast heating rate of 10 °C min^{-1} and with a nitrogen gas flow was applied. During the treatment, sulfur powder was vaporized and reacted with the electrode. The residual sulfur in the boat was removed along with the nitrogen gas flow. The residual area of the stainless-steel mesh current collector was removed by the hole puncher with a diameter of 8 mm. Due to the similar molar mass of MnO_2 and MnS, the resulting areal MnS loading amount is same to that of MnO_2 (~2-3 mg cm^{-2}). The areal loading amount of the $Ni_xCo_{1-x}S_2$ was evaluated based on the weight differences before and after the electrodeposition of NiCo-LDH and on the molar weight relationship between NiCo-LDH and $Ni_xCo_{1-x}S_2$. For a 300s deposition, areal loading amount of the resulting $Ni_xCo_{1-x}S_2$ was ~0.8 mg cm^{-2}. For comparison purpose, a single layer electrode with Pt/C + IrO_2 (4 mg cm^{-2} with a mass ratio of Pt/C:IrO_2 = 1:1), CNT and PTFE (with a mass ratio of catalyst:CNT:PTFE = 6:2:2) was also prepared following procedures similar to those for the MnO_2-CNT-PTFE film.

Characterizations: Phase structure of the samples was analyzed with XRD (Bruker D8 Advance, Cu Kα radiation) and HR-TEM (Titan G2). The hydrophilicity and hydrophobicity of the electrodes were evaluated using the contact angle test with the Zn-based battery electrolyte (6 M KOH + 0.2 M Zn(Ac)$_2$). The texture, morphology and elemental dispersion of the double-layer electrode was

analyzed with a SEM (Zeiss) equipped with an EDS function. High-resolution elemental dispersion on the electrode layers was further analyzed with the EDS mapping function equipped on the Titan G2.

Evaluation of oxygen catalytic activity: The electrocatalytic ORR and OER performance of the powder samples was assessed by a three-electrode setup with RDE as working electrode (Pine Research Instrumentation). A Pt wire, a Ag/AgCl (4 M KCl) electrode and 0.1 M KOH aqueous solution was used as counter, reference electrode and electrolyte, respectively. The area of the glassy carbon of the RDE was 0.196 cm^2 and the mass loading of the catalyst was 0.232 mg cm^{-2}. A dispersion containing 10 mg of catalyst, 10 mg of conductive carbon (Super P Li), 1 mL of ethanol and 0.1 mL of 5% Nafion®117 solution was prepared by ultrasonic mixing of the materials in an ultrasonic bath. Pt/C + IrO_2 mixture (1:1, wt:wt) was also evaluated for comparisons. The mixture contains 5 mg of 20% Pt/C, 5 mg of IrO_2 and 10 mg of Super P. 5 µL dispersion was drop-casted on the glassy carbon area of the RDE. The electrolyte was purged with pure oxygen for 0.5 h before test and continual oxygen bubbling was kept during the tests. Electrochemical results were recorded using a potentiostat (CH Instruments CHI760E). Linear sweep voltammetry (LSV) profiles were collected at a rotation speed of 1600 rpm with a scan rate of 5 mV s^{-1}. A negative scan from 0.2 to -0.60 V vs. Ag/AgCl was applied for evaluating the ORR activity and a positive scan from 0.2 to 1.00 V vs. Ag/AgCl for the OER activity. Potentials in the RDE evaluation are presented in the RHE scale, which was converted from the measured potential (vs. Ag/AgCl) by the equation: $E(RHE) = E(Ag/AgCl) + 0.199 + 0.0591 \times pH$. Ohmic losses were considered by subtracting the voltage drop from the potentials. A resistance of ~45 Ω measured by electrochemical impedance spectroscopy (EIS) of the working electrode was used for determining the ohmic voltage drop. To evaluate the electron transfer number (n) and peroxide yield (X, percentage of HO_2^- to the total reduced products) of the catalyst, rotating ring-disk electrode (RRDE) setup was applied. The working electrode (AFE7R9GCPT, Pine Instruments) consists of a Pt ring (inner diameter: 6.25 mm; outer diameter: 7.92 mm) and a glassy carbon disk (5.61 mm diameter) with a collection efficiency (N) determined to be 37%. The

disk electrode was negatively scanned at the rate of 5 mV s^{-1} from 0.2 to -0.6 V (vs Ag/AgCl), while the ring electrode was settled at a constant potential of 0.5 V (vs Ag/AgCl). The value of n and X were calculated by the following equations:

$$n = 4 \times \frac{I_d}{I_d + I_r/N}$$

$$X = 200 \times \frac{I_r/N}{I_d + I_r/N}$$

Where I_d, I_r and N referred to the disk current, ring current and collection efficiency.

Assembling and evaluation of hybrid Zn batteries: The as-prepared function-separated electrodes (diameter of 8 mm) was put in the center of a carbon gas diffusion layer (GDL, AVCarb P75T, 1.5×1.5 cm) and then put on a stainless-steel mesh (1.5×1.5 cm), then cold pressed with a 4 MPa pressure. A home-made Zn-air battery model was utilized for the electrochemical evaluation of the hybrid Zn battery with a Zn plate as anode and an 6 M KOH + 0.2 M Zn(Ac)$_2$ as electrolyte. Cyclic voltammetry (CV) scans of the hybrid Zn batteries were recorded using a Biologic VSP potentiostat. Galvanostatic charging and discharging profiles and cycling stability of the batteries were recorded using a LANHE CT2001A battery test system.

Supporting Information

Supporting Information is available from the Wiley Online Library or from the author.

Conflict of Interest

The authors declare no conflict of interest.

Received: ((will be filled in by the editorial staff))
Revised: ((will be filled in by the editorial staff))
Published online: ((will be filled in by the editorial staff))

References

[1]   B. Dunn, H. Kamath, J.-M. Tarascon, *Science* **2011**, *334*, 928.

[2]   Z. Yang, J. Zhang, M. C. W. Kintner-Meyer, X. Lu, D. Choi, J. P. Lemmon, J. Liu, *Chem. Rev.* **2011**, *111*, 3577.

[3]   Q. Zhao, S. Stalin, C.-Z. Zhao, L. A. Archer, *Nat. Rev. Mater.* **2020**, *5*, 229.

[4]   H. Yang, Z. Chang, Y. Qiao, H. Deng, X. Mu, P. He, H. Zhou, *Angew. Chem. Int. Ed.* **2020**, *59*, 9377.

[5]   Y.-P. Deng, R. Liang, G. Jiang, Y. Jiang, A. Yu, Z. Chen, *ACS Energy Lett.* **2020**, *5*, 1665.

[6]   Y. Li, J. Lu, *ACS Energy Lett.* **2017**, *2*, 1370.

[7]   J. Yu, R. Ran, Y. Zhong, W. Zhou, M. Ni, Z. Shao, *Energy Environ. Mater.* **2020**, *3*, 121.

[8]   Y. Zhong, X. Xu, W. Wang, Z. Shao, *Batteries Supercaps* **2019**, *2*, 272.

[9]   J. Fu, Z. P. Cano, M. G. Park, A. Yu, M. Fowler, Z. Chen, *Adv. Mater.* **2017**, *29*, 1604685.

[10]   Q. Lu, Y. Guo, P. Mao, K. Liao, X. Zou, J. Dai, P. Tan, R. Ran, W. Zhou, M. Ni, Z. Shao, *Energy Storage Mater.* **2020**, *32*, 20.

[11]   W. Shang, W. Yu, Y. Liu, R. Li, Y. Dai, C. Cheng, P. Tan, M. Ni, *Energy Storage Mater.* **2020**, *31*, 44.

[12]   X. Wang, F. Wang, L. Wang, M. Li, Y. Wang, B. Chen, Y. Zhu, L. Fu, L. Zha, L. Zhang, Y. Wu, W. Huang, *Adv. Mater.* **2016**, *28*, 4904.

[13]   L. Li, L. Jiang, Y. Qing, Y. Zeng, Z. Zhang, L. Xiao, X. Lu, Y. Wu, *J. Mater. Chem. A* **2020**, *8*, 565.

[14]   W. Shang, W. Yu, P. Tan, B. Chen, Z. Wu, H. Xu, M. Ni, *J. Mater. Chem. A* **2019**, *7*, 15564.

WILEY-VCH

[15]   D. U. Lee, J. Fu, M. G. Park, H. Liu, A. Ghorbani Kashkooli, Z. Chen, *Nano Lett.* **2016**, *16*, 1794.

[16]   B. Li, J. Ruan, A. Loh, J. Chai, Y. Chen, C. Tan, X. Ge, T. S. A. Hor, Z. Liu, H. Zhang, Y. Zong, *Nano Lett.* **2017**, *17*, 156.

[17]   L. Ma, S. Chen, Z. Pei, H. Li, Z. Wang, Z. Liu, Z. Tang, J. A. Zapien, C. Zhi, *ACS Nano* **2018**, *12*, 8597.

[18]   P. Tan, B. Chen, H. Xu, W. Cai, W. He, M. Liu, Z. Shao, M. Ni, *Small* **2018**, *14*, 1800225.

[19]   D. Xu, S. Wu, X. Xu, Q. Wang, *ACS Sustainable Chem. Eng.* **2020**, *8*, 4384.

[20]   Y. Cheng, N. Zhang, Q. Wang, Y. Guo, S. Tao, Z. Liao, P. Jiang, Z. Xiang, *Nano Energy* **2019**, *63*, 103822.

[21]   P. Tan, B. Chen, H. Xu, W. Cai, M. Liu, Z. Shao, M. Ni, *J. Electrochem. Soc.* **2018**, *165*, A2119.

[22]   M. Wu, G. Zhang, N. Chen, W. Chen, J. Qiao, S. Sun, *Energy Storage Mater.* **2020**, *24*, 272.

[23]   X. Wang, X. Xu, J. Chen, Q. Wang, *ACS Sustainable Chem. Eng.* **2019**, *7*, 12331.

[24]   S. Sarawutanukul, C. Tomon, S. Duangdangchote, N. Phattharasupakun, M. Sawangphruk, *Batteries Supercaps* **2020**, *3*, 541.

[25]   C.-C. Chang, Y.-C. Lee, H.-J. Liao, Y.-T. Kao, J.-Y. An, D.-Y. Wang, *ACS Sustainable Chem. Eng.* **2019**, *7*, 2860.

[26]   P. Tan, B. Chen, H. Xu, W. Cai, W. He, H. Zhang, M. Liu, Z. Shao, M. Ni, *ACS ACS Appl. Mater. Interfaces* **2018**, *10*, 36873.

[27]   Z. Huang, X. Li, Q. Yang, L. Ma, F. Mo, G. Liang, D. Wang, Z. Liu, H. Li, C. Zhi, *J. Mater. Chem. A* **2019**, *7*, 18915.

WILEY-VCH

[28] S. Khaja Hussain, J. Su Yu, *Chem. Eng. J.* **2019**, *361*, 1030.

[29] A. Qaseem, F. Chen, C. Qiu, A. Mahmoudi, X. Wu, X. Wang, R. L. Johnston, *Part. Part. Syst. Char.* **2017**, *34*, 1700097.

[30] L. Meng, D. Lin, J. Wang, Y. Zeng, Y. Liu, X. Lu, *ACS Appl. Mater. Interfaces* **2019**, *11*, 14854.

[31] J. Yu, B.-Q. Li, C.-X. Zhao, J.-N. Liu, Q. Zhang, *Adv. Mater.* **2020**, *32*, 1908488.

[32] T. Zhou, N. Zhang, C. Wu, Y. Xie, *Energy Environ. Sci.* **2020**, *13*, 1132.

[33] C. Lin, S. S. Shinde, Z. Jiang, X. Song, Y. Sun, L. Guo, H. Zhang, J.-Y. Jung, X. Li, J.-H. Lee, *J. Mater. Chem. A* **2017**, *5*, 13994.

[34] X. Song, L. Guo, X. Liao, J. Liu, J. Sun, X. Li, *Small* **2017**, *13*, 1700238.

[35] Z. Li, G. Jiang, Y.-P. Deng, G. Liu, D. Ren, Z. Zhang, J. Zhu, R. Gao, Y. Jiang, D. Luo, Y. Zhu, D.-H. Liu, A. M. Jauhar, H. Jin, Y. Hu, S. Wang, Z. Chen, *iScience* **2020**, *23*, 101404.

[36] Y. Lu, J. Wang, S. Zeng, L. Zhou, W. Xu, D. Zheng, J. Liu, Y. Zeng, X. Lu, *J. Mater. Chem. A* **2019**, *7*, 21678.

[37] W. Tian, H. Li, B. Qin, Y. Xu, Y. Hao, Y. Li, G. Zhang, J. Liu, X. Sun, X. Duan, *J. Mater. Chem. A* **2017**, *5*, 7103.

[38] J. Pan, Y. Y. Xu, H. Yang, Z. Dong, H. Liu, B. Y. Xia, *Adv. Sci.* **2018**, *5*, 1700691.

[39] X. Cai, L. Lai, J. Lin, Z. Shen, *Mater. Horiz.* **2017**, *4*, 945.

[40] H. Zhang, Y. Zhao, Y. Li, G. Li, J. Li, F. Zhang, *ACS Appl. Energy Mater.* **2020**, *3*, 705.

[41] X. Meng, X. Deng, L. Zhou, B. Hu, W. Tan, W. Zhou, M. Liu, Z. Shao, *Energy Environ. Mater.* **2020**, in press. DOI: 10.1002/eem2.12105

WILEY-VCH

[42] Y. Li, H. Zhang, N. Han, Y. Kuang, J. Liu, W. Liu, H. Duan, X. Sun, *Nano Res.* **2019**, *12*, 177.

[43] P. Wang, Y. Lin, L. Wan, B. Wang, *ACS Appl. Mater.* Interfaces **2019**, *11*, 37701.

[44] L. Wan, P. Wang, Y. Lin, B. Wang, *J. Electrochem. Soc.* **2019**, *166*, A3409.

[45] C. Yuan, J. Li, L. Hou, X. Zhang, L. Shen, X. W. Lou, *Adv. Funct. Mater.* **2012**, *22*, 4592.

[46] L. Huang, D. Chen, Y. Ding, S. Feng, Z. L. Wang, M. Liu, *Nano Lett.* **2013**, *13*, 3135.

[47] H. H. Heikens, C. F. Van Bruggen, C. Haas, *J. Phys. Chem. Solids* **1978**, *39*, 833.

[48] R. N. De Guzman, A. Awaluddin, Y.-F. Shen, Z. R. Tian, S. L. Suib, S. Ching, C.-L. O'Young, *Chem. Mater.* **1995**, *7*, 1286.

[49] X. Xu, W. Wang, W. Zhou, Z. Shao, *Small Methods* **2018**, *2*, 1800071.

[50] Z. Pei, Z. Yuan, C. Wang, S. Zhao, J. Fei, L. Wei, J. Chen, C. Wang, R. Qi, Z. Liu, Y. Chen, *Angew. Chem. Int. Ed.* **2020**, *59*, 4793.

[51] T. Tang, W.-J. Jiang, X.-Z. Liu, J. Deng, S. Niu, B. Wang, S.-F. Jin, Q. Zhang, L. Gu, J.-S. Hu, L.-J. Wan, *J. Am. Chem. Soc.* **2020**, *142*, 7116.

[52] Y. Arafat, M. R. Azhar, Y. Zhong, X. Xu, M. O. Tadé, Z. Shao, *Nano-Micro Lett.* **2020**, *12*, 130.

[53] Q. Lu, X. Zou, K. Liao, R. Ran, W. Zhou, M. Ni, Z. Shao, *Carbon Energy,* **2020**, *2*, 461.

[54] L. Zhang, H. B. Wu, X. W. Lou, *Chem. Commun.* **2012**, *48*, 6912.

[55] L. Jin, B. Liu, Y. Wu, S. Thanneeru, J. He, *ACS Appl. Mater. Interfaces* **2017**, *9*, 36837.

[56] S. Peng, L. Li, H. Tan, R. Cai, W. Shi, C. Li, S. G. Mhaisalkar, M. Srinivasan, S. Ramakrishna, Q. Yan, *Adv. Funct. Mater.* **2014**, *24*, 2155.

[57]   Y. Ruan, J. Jiang, H. Wan, X. Ji, L. Miao, L. Peng, B. Zhang, L. Lv, J. Liu, *J. Power Sources* **2016**, *301*, 122.

[58]   Y. F. Tang, T. Chen, S. X. Yu, *Chem. Commun.* **2015**, *51*, 9018.

[59]   Y. F. Tang, T. Chen, S. X. Yu, Y. Q. Qiao, S. C. Mu, J. Hu, F. M. Gao, *J. Mater. Chem. A* **2015**, *3*, 12913.

[60]   A. Kozawa, J. F. Yeager, *J. Electrochem. Soc.* **1965**, *112*, 959.

[61]   A. Kozawa, J. F. Yeager, *J. Electrochem. Soc.* **1968**, *115*, 1003.

[62]   Y. Zhong, X. Xu, J.-P. Veder, Z. Shao, *iScience* **2020**, *23*, 100943.

[63]   W. Liu, J. Zhang, Z. Bai, G. Jiang, M. Li, K. Feng, L. Yang, Y. Ding, T. Yu, Z. Chen, A. Yu, *Adv. Funct. Mater.* **2018**, *28*, 1706675.

[64]   J. Yin, Y. Li, F. Lv, M. Lu, K. Sun, W. Wang, L. Wang, F. Cheng, Y. Li, P. Xi, S. Guo, *Adv. Mater.* **2017**, *29*, 1704681.

[65]   X. Han, W. Zhang, X. Ma, C. Zhong, N. Zhao, W. Hu, Y. Deng, *Adv. Mater.* **2019**, *31*, 1808281.

[66]   Q. Lu, J. Yu, X. Zou, K. Liao, P. Tan, W. Zhou, M. Ni, Z. Shao, *Adv. Funct. Mater.* **2019**, *29*, 1904481.

[67]   A. Pendashteh, J. S. Sanchez, J. Palma, M. Anderson, R. Marcilla, *Energy Storage Mater.* **2019**, *20*, 216.

[68]   Y.-P. Deng, Y. Jiang, R. Liang, S.-J. Zhang, D. Luo, Y. Hu, X. Wang, J.-T. Li, A. Yu, Z. Chen, *Nat. Commun.* **2020**, *11*, 1952.

[69]   Y. Li, M. Gong, Y. Liang, J. Feng, J.-E. Kim, H. Wang, G. Hong, B. Zhang, H. Dai, *Nat. Commun.* **2013**, *4*, 1805.

[70]   Y. Cheng, S. Dou, J.-P. Veder, S. Wang, M. Saunders, S. P. Jiang, *ACS Appl. Mater. Interfaces* **2017**, *9*, 8121.

[71]   N. Xu, Y. Zhang, M. Wang, X. Fan, T. Zhang, L. Peng, X.-D. Zhou, J. Qiao, *Nano Energy* **2019**, *65*, 104021.

[72]   X. Wang, J. Sunarso, Q. Lu, Z. Zhou, J. Dai, D. Guan, W. Zhou, Z. Shao, *Adv. Energy Mater.* **2020**, *10*, 1903271.
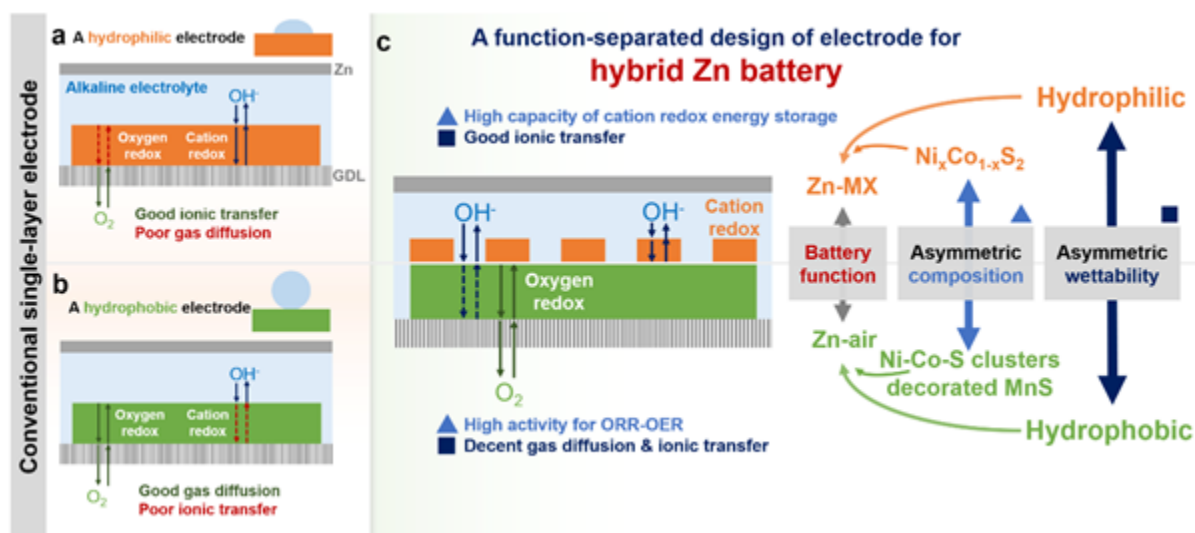
Figure 1. Schematic illustrations of the function-separated design of electrode for hybrid Zn battery. a,b) conventional single-layer electrodes with a) a hydrophilic surface and b) a hydrophobic surface; c) the advantages for facilitating redox reactions and mass transfers in different layers of a function-separated MnS-$Ni_xCo_{1-x}S_2$ electrode, respectively.
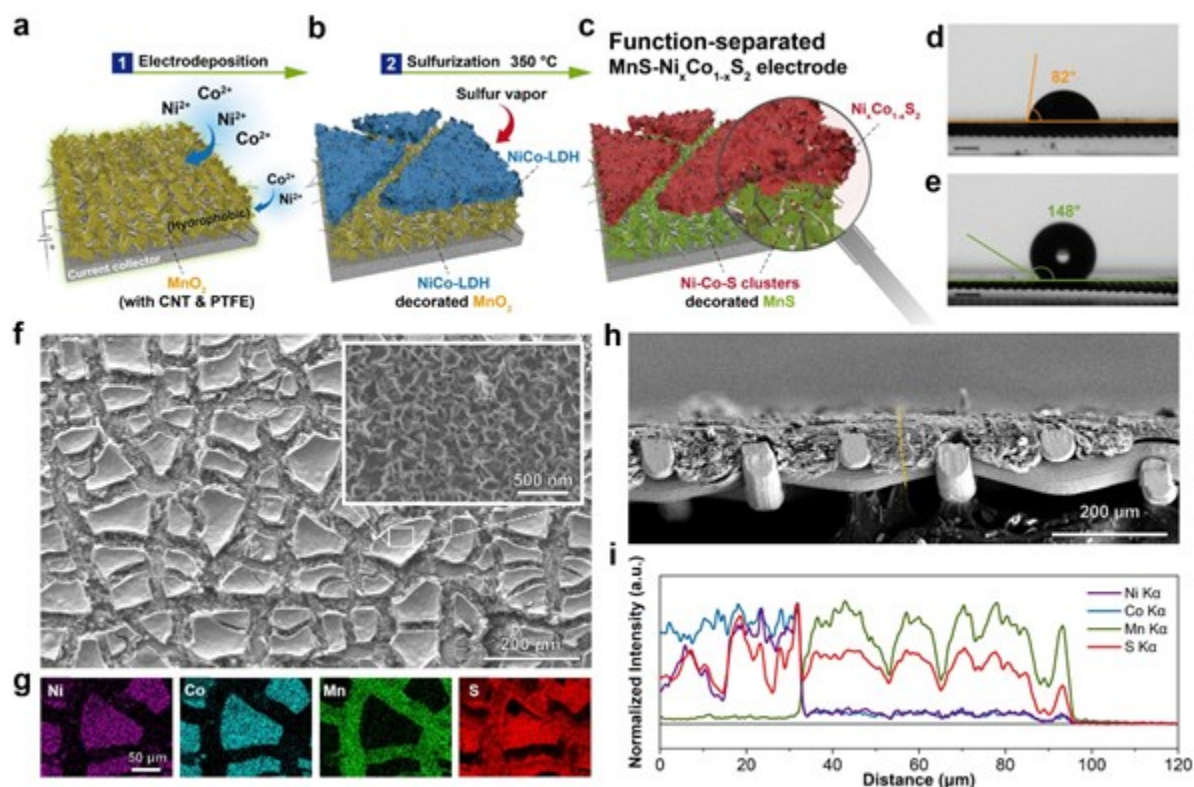
Figure 2. Preparation and characterization of the function-separated MnS-$Ni_xCo_{1-x}S_2$ electrode. a-c) Illustration of the preparing process; d-e) Wettability characteristics evaluated by the contact angles analysis with the hybrid battery electrolyte on d) hydrophilic $Ni_xCo_{1-x}S_2$ layer and e) hydrophobic MnS layer; f) SEM of the function-separated MnS-$Ni_xCo_{1-x}S_2$ electrode (inset image shows the porous structure of the hydrophilic $Ni_xCo_{1-x}S_2$ layer) and g) EDS element mapping; h) SEM of the cross-section of the function-separated MnS-$Ni_xCo_{1-x}S_2$ electrode and i) EDS linear scan analysis across the layers.
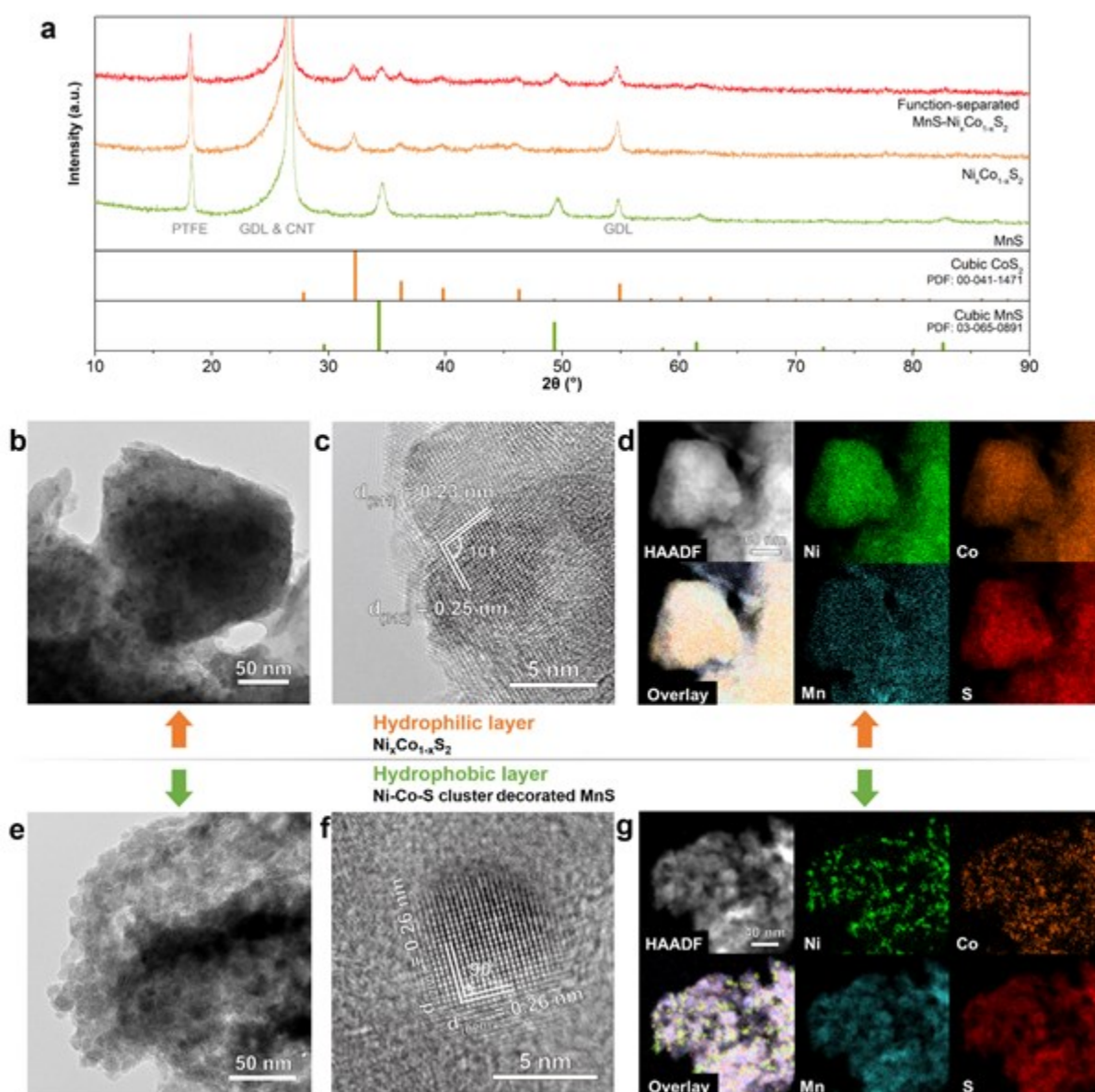
23

Figure 3. Structural and compositional characterization of the function-separated MnS-Ni$_x$Co$_{1-x}$S$_2$ electrode. a) XRD profiles of function-separated MnS-Ni$_x$Co$_{1-x}$S$_2$ electrode compared with two electrodes with only MnS or Ni$_x$Co$_{1-x}$S$_2$; b) TEM and c) HR-TEM observation and d) TEM-EDS elemental mapping of the hydrophilic layer; e) TEM and f) HR-TEM observation and g) TEM-EDS elemental mapping of the hydrophobic layer.
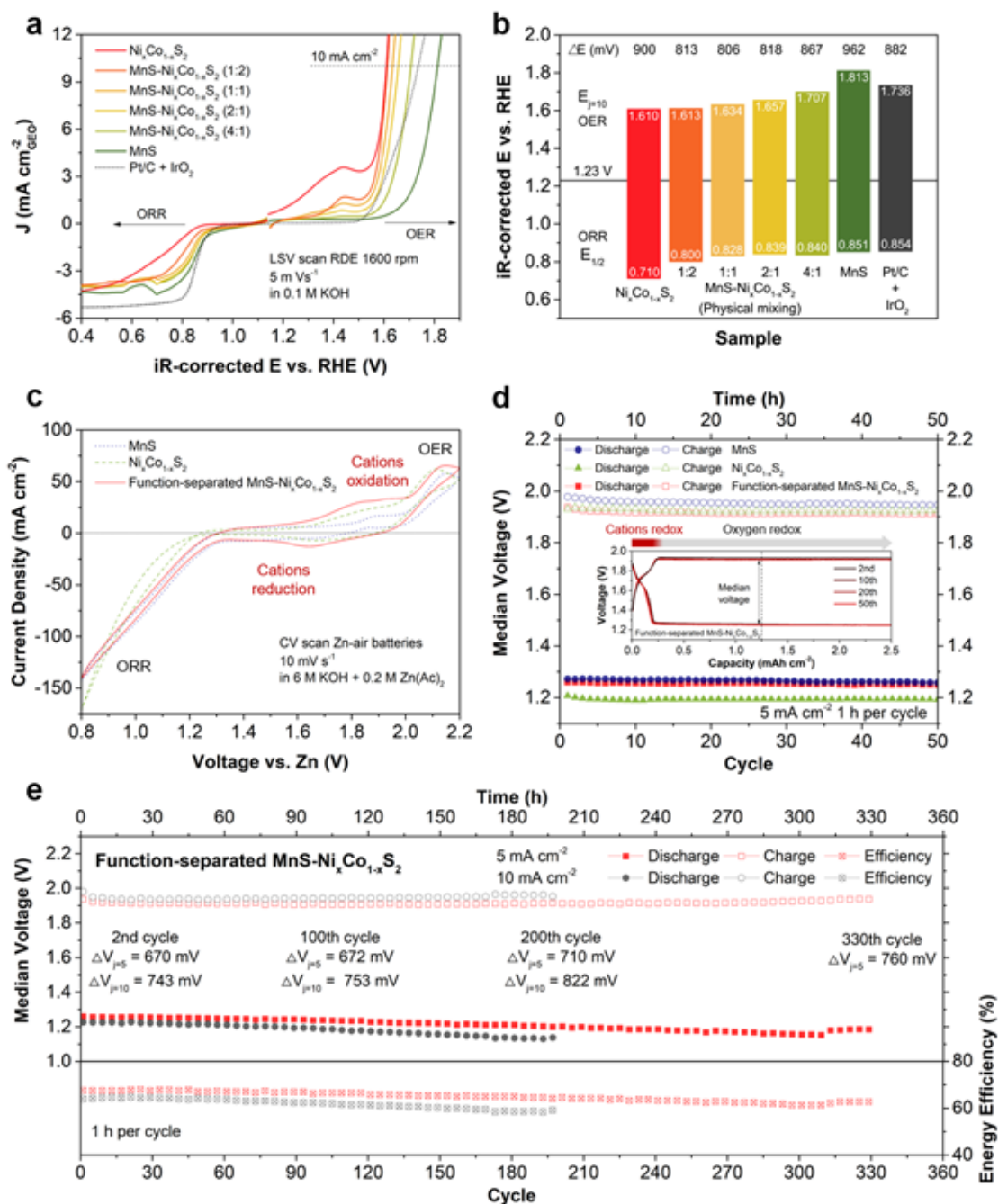
24

Figure 4. Bifunctional catalytic activity of MnS and $Ni_xCo_{1-x}S_2$ materials and performance of the Zn-air battery function of the function-separated MnS-$Ni_xCo_{1-x}S_2$ electrode. a) ORR and OER polarization curves of MnS, $Ni_xCo_{1-x}S_2$ materials and their physical mixture compared with commercial Pt/C + IrO_2, b) the corresponding potential gaps (ΔE) between potential at 10 mA cm^{-2} ($E_{j=10}$) for OER and the half-wave potential ($E_{1/2}$) for ORR; c) CV scan profiles of the hybrid Zn battery with function-separated MnS-$Ni_xCo_{1-x}S_2$ electrode compared with electrodes with only MnS or $Ni_xCo_{1-x}S_2$; d) variation of the median discharge and charge voltages over 50 cycles of the batteries at 5 mA cm^{-2}; e) cycling stabilities at 5 and 10 mA cm^{-2}.
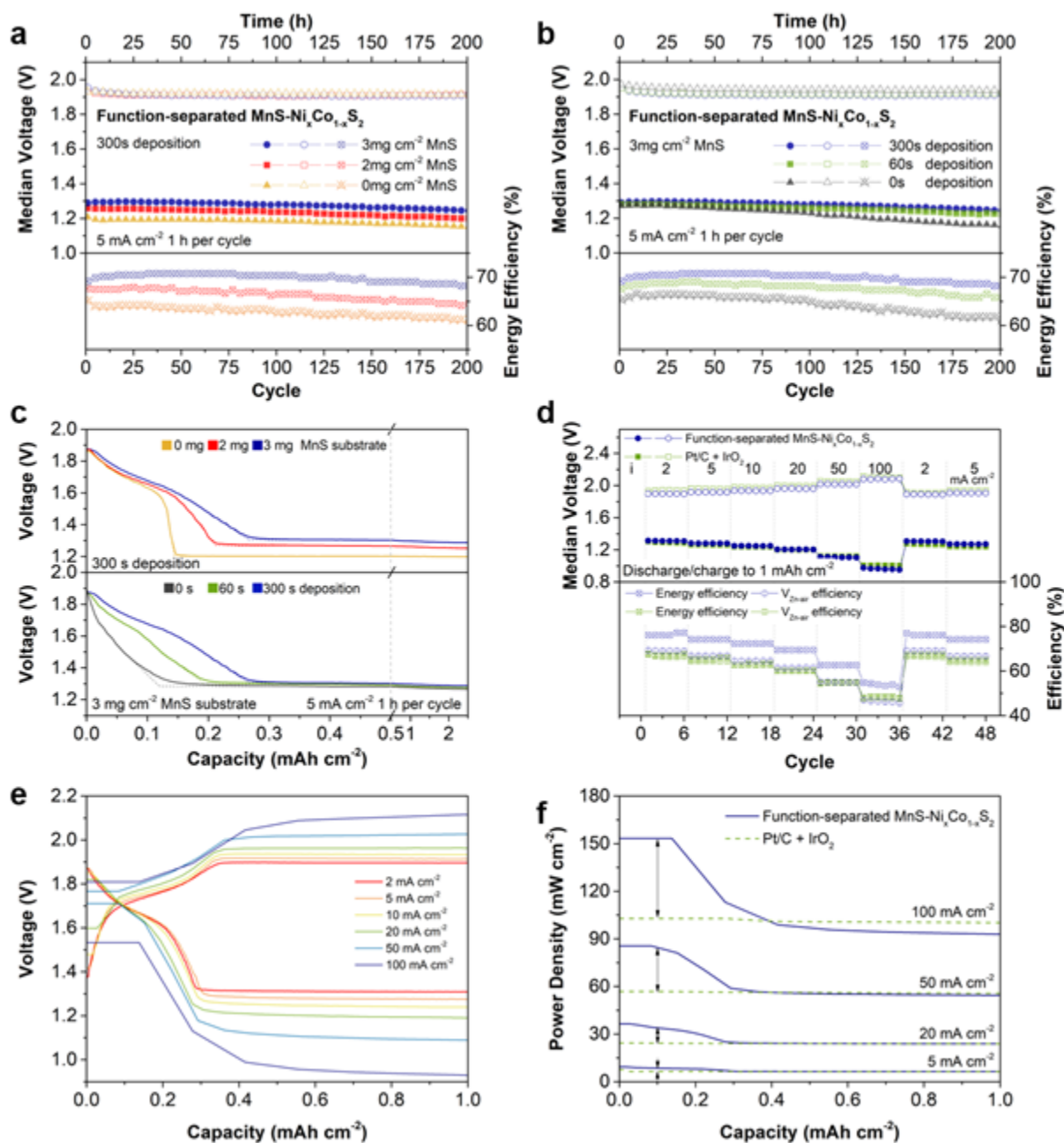
25

Figure 5. Performance of the Zn-MX battery function and optimization of the function-separated MnS-Ni$_x$Co$_{1-x}$S$_2$ electrode. a) Comparison of cycling performance of cathodes with different mass loading of MnS and b) with different amount of Ni$_x$Co$_{1-x}$S$_2$ by appling different deposition time. c) Comparison of capacities of the Zn-MX battery function of cathodes with different MnS and Ni$_x$Co$_{1-x}$S$_2$ loading. d) Variation of median discharge and charge voltages for the optimized electrode at current densities ranging from 2 to 100 mA cm^{-2}, e) the corresponding single cycle charge-discharge profiles and f) variation of power densities along with the capacity evaluated at different constant current densities.
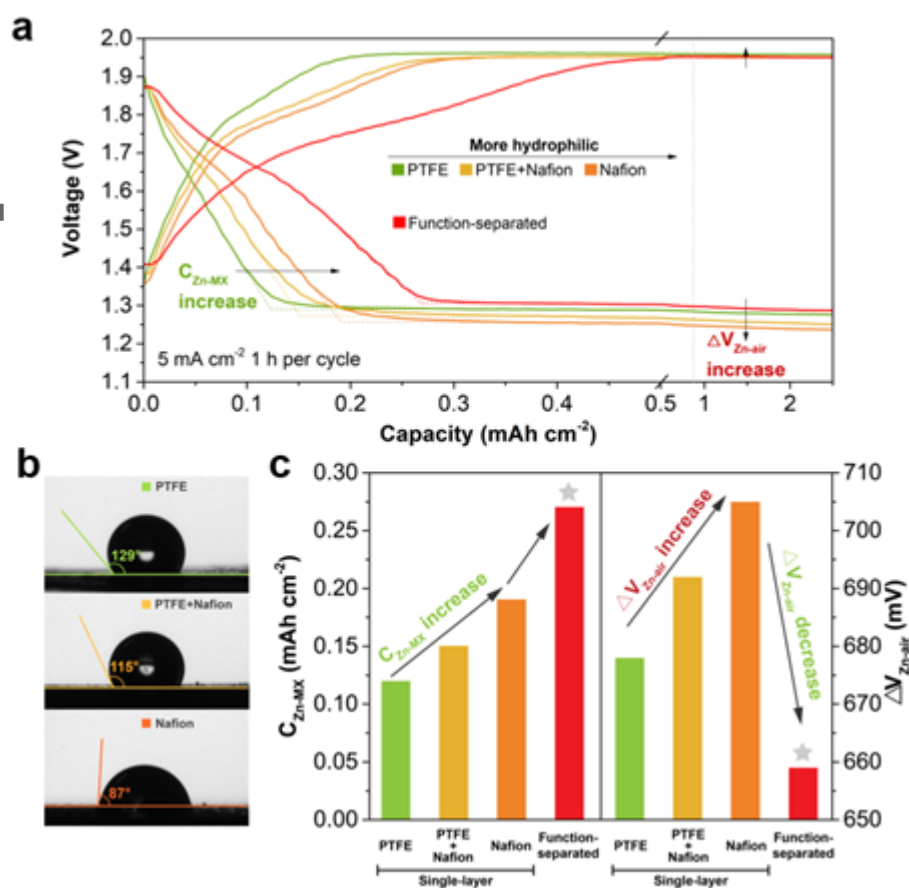
Figure 6. Verification of the important role of the asymmetric wettability design of the function-separation MnS-Ni$_x$Co$_{1-x}$S$_2$ electrode. a) Second charge-discharge profiles of three hybrid Zn-based batteries with conventional single-layer MnS-Ni$_x$Co$_{1-x}$S$_2$ electrode with different wettability and the function-separated MnS-Ni$_x$Co$_{1-x}$S$_2$ electrode. b) contact angles analysis on the electrode with different wettability tuning agents with the hybrid Zn battery electrolyte. c) Comparison of hybrid Zn-based batteries performance based on the two essential parameters, i.e., capacity of the Zn-MX battery function (C$_{Zn-MX}$, mAh cm^{-2}) and charge-discharge voltage gap of the Zn-air battery function (ΔV$_{Zn-air}$, mV vs. Zn).

An electrode with a function-separated design is developed for hybrid zinc batteries. The electrode composes of a hydrophobic MnS layer decorated with Ni-Co-S nanoclusters that allows smooth gas diffusion and efficient oxygen electrocatalysis and a hydrophilic $Ni_xCo_{1-x}S_2$ layer that favors fast ionic transfer and superior performance for energy storage. The battery shows excellent rate performance, round-trip efficiency and cycling stability.

Y. Zhong, X. Xu, P. Liu, R. Ran, S. P. Jiang, H. Wu, Z. Shao*

A function-separated design of electrode for realizing high-performance hybrid zinc battery